Polyelectrolyte-Directed Nanoparticle Aggregation: Systematic Morphogenesis of Calcium Carbonate by Nonclassical Crystallization

Rui-Qi Song,[†] Helmut Cölfen,[†,*] An-Wu Xu,[‡] Jürgen Hartmann,[†] and Markus Antonietti[†]

[†]Department of Colloid Chemistry, Max Planck Institute of Colloids and Interfaces, Research Campus Golm, 14424 Potsdam, Germany, and [‡]Division of Nanomaterials and Chemistry, Hefei National Laboratory for Physical Sciences at Microscale Department, University of Science and Technology of China, Hefei 230026, China

ABSTRACT Besides the classical atom/ion/molecule based mechanism, nonclassical crystallization provides a nanoparticle-based crystallization pathway toward single crystals. However, there is a lack of experimentally established strategies for engineering a range of crystalline microstructures from common nanoparticles by nonclassical crystallization. We demonstrate that a commercial random copolymer polyelectrolyte poly(4-styrene sulfonate)-*co*-(maleic acid) (PSS-*co*-MA) considerably guides crystallization of calcium carbonate (CC) with a high versatility. The bioinspired nonclassical crystallization protocol yielded a series of calcite microstructures. Calcite single crystals obtained at low supersaturation show a pseudo-dodecahedral shape with curved faces, whereas increasing supersaturation generated calcite mesocrystals with pseudo-octahedral shapes and scalloped surfaces. Further increase of supersaturation induced the formation of polycrystalline multilayered and hollow spheres. In the initial growth stage of all these microstructures, amorphous CC nanoparticles formed as the early product. Remarkably, microparticles with minimal primitive (P)-surface were captured as the prominent intermediate indicative of liquidlike behavior. Moreover, nanogranular structures exist broadly in the as-synthesized crystals. These results demonstrate that the polyelectrolyte can effectively stabilize the amorphous CC nanoparticle precursors, impart control over the evolution from amorphous precursors *via* a liquid aggregate through P-surface intermediates to the final crystals, and thus allow the morphogenesis. Simple variation of calcium and polyeletrolyte concentrations enables a systematic control over the size and morphology of particles among pseudo-dodecahedra, pseudo-octahedra, multilayered spheres, and hollow spheres, which are expressed in a morphology diagram. A unifying nanoparticle aggregation formation mechanism was suggested to explain the morphogenesis by the combination of nonclassical crystallization and surface area minimization principles.

*Address correspondence to coelfen@mpikg.mpg.de.

Controlled nanoparticle aggregation is a topic of considerable scientific interest in nanotechnology and materials science. Serving as a bottom-up assembly scheme, it possesses two major advantages for the fabrication of novel materials. First, assembling nanoscale building blocks allows utilization of the interactions between the constituents to precisely engineer crystal shapes that can not be realized *via* a classical atom/ion/molecule-based crystallization technique mainly due to the inherent crystal anisotropy.[1−5] Sec-

ond, combining nanoparticles of different materials and inorganic−organic hybrids can provide a large number of possibilities to rationally tailor desired properties of a material by the simple composition regulation.[6,7] Inspired by nature's great control over the placement of nanoscale building blocks for the formation of mesoscopic and macroscopic aggregates, nanoparticle oriented attachment[8−12] and gel matrix-mediated nanoparticle arrangement[13−16] evidenced enormous advances. However, it is still a great challenge to obtain ultimate control over nanoparticle aggregation to assemble microstructures with shapes and properties tailored for a given application. Also it is currently hard to predict the assembly route of nanoparticles for a given set of conditions.

Polyelectrolytes are polymers with repeating units bearing charged groups, which can dissociate from their counterions in water. Fascinated by the polymer controlled production of calcium carbonate (CC) biominerals in a wide variety of biological systems in nature, many groups applied polyelectrolytes to modify CC crystallization in order to pursue possible access to mimicking the growth of natural biominerals. The composition, conformation, charge density, pH, and solvent dependence of polyelectrolytes are variables to modulate their interactions with growing crystal species and thus the morphogenesis. It turned out that CC single crystals, such as calcite and vaterite, are scarcely available in polyelectrolyte controlled crystallization, though polyelectrolytes can temporarily stabilize amorphous calcium carbonate (ACC) precursor nanoparticles

and inhibit the growth of individual particles.[17−25] Subject to energetic constraints, particles usually aggregate to polycrystalline microparticles. This aggregation process can be controlled, which opens up an alternative crystallization pathway: nanoparticle-mediated crystallization (nonclassical crystallization) in contrast to atom or molecule-mediated conventional crystallization. This pathway yields mesoscopically ordered assemblies of nanoparticles, which can finally fuse to a single crystal.[26−29] Poly(sodium 4-styrenesulfonate) (PSS),[30,31] poly(styrene-*alt*-maleic acid) (PS-MA),[32] and poly(ethylene oxide)-*block*-poly(styrene sulfonate) PEO-*b*-PSS[33] have been shown to enable the formation of calcite mesocrystals with rough surfaces and porous structures. Although crystallization pathways to polycrystalline aggregates, single crystals, and mesocrystals were found to belong to a unifying framework based on the aggregation of precursor subunits,[33] most CC products obtained so far seem to be only serendipitous parts of a more complex crystallization scenario. Hitherto, the systematic precise control over CC crystallization, from one and the same solution system without any chemical variation, was only rarely reported.[20,33]

Furthermore, such systematic morphogenesis studies are an important first step to harness the potential of utilizing polyelectrolytes as crystal growth modifier and to access bioinspired superstructure construction principles that can be integrated into existing crystallization principles.

Here, we approached the nanoparticle-mediated construction of calcite particles with microstructures ranging from single crystalline, *via* mesocrystals to polycrystalline by controlling nanoparticle aggregation with a commercial polyelectrolyte, poly(4-styrenesulfonate-*co*-maleic acid) (PSS-*co*-MA) random copolymer, as the crystal modifier in detail following a preliminary investigation of calcite crystals, which are accessible with this polymer.[34] Although most polyelectrolytes used to effectively control crystallization of CC are block copolymers consisting of two or more homopolymer subunits linked together by covalent bonds, we chose a copolymer with random sequences of styrenesulfonate and maleic acid monomers. Carboxylate groups of small dicarboxylic acid molecules have been reported to modulate crystal morphology by inhibiting crystal growth upon binding to the {110} planes.[35] Sulfonate groups on the other hand are able to control the morphology of calcite mesocrystals by stabilization of the {001} planes.[30−32] It is reasonable to assume that a random copolymer consisting of these two surface-active monomers can bind to both fami-
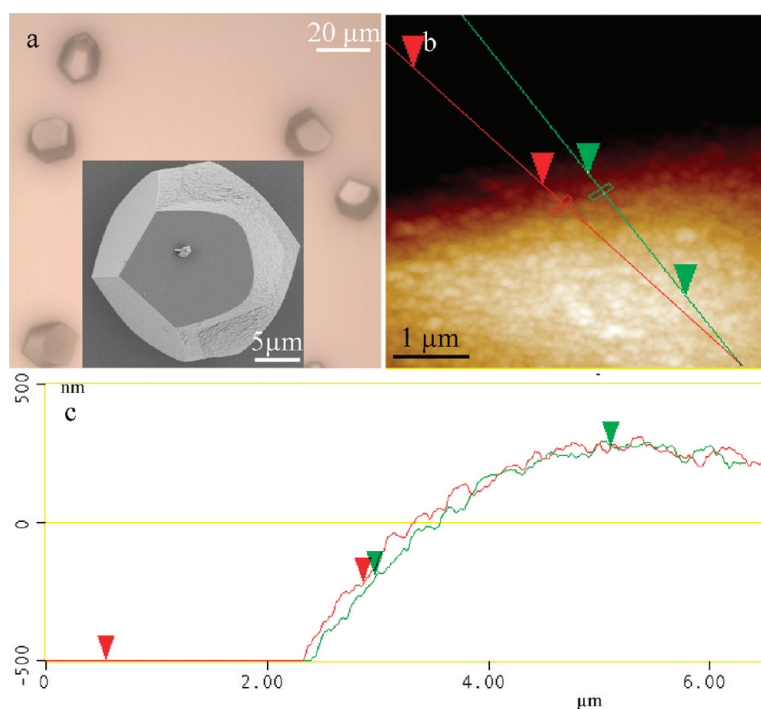

Figure 1. Calcite pseudo-dodecahedral particles: (a) optical microscopy image of particles in solution, (inset of panel a) SEM image of a typical pseudo-dodecahedral particle; (b) AFM height image (5 × 5 μm) of rough faces on the selected calcite pseudo-dodecahedral particle; and (c) section analysis showing the curvature of the rough face in panel b. [PSS-*co*-MA] = 0.1 g/L, [CaCl₂] = 1.25 mM, 2 weeks.

lies of faces and thus would have a very effective influence on the nucleation and growth, orientation, and morphology of CC crystals. Moreover, the inherent conformational flexibility of PSS-*co*-MA provides an opportunity to control a wide range of crystal structures by the same mechanism without altering the chemical nature of the system.

RESULTS AND DISCUSSION

Calcite Single Crystals. We started the systematic work with low concentration of PSS-*co*-MA in diluted CaCl₂ solution. Crystallization of CC through a gas-diffusion procedure in CaCl₂ solution (1.25 mM) with PSS-*co*-MA (0.1 g/L) as additive produced calcite single crystals with pseudo-dodecahedral shapes after 2 weeks, as shown in Figure 1.

An optical microscope image of the obtained product in Figure 1a shows that the sample is composed of particles that are uniform in shape: their external morphologies display pseudo-dodecahedral shapes with an edge size of 20−30 μm. Some particles with multiple-twinned structures or ill-defined structures with elongated tips can also be found in the product. From the typical SEM images of individual particles,[34] it can be observed that there is a total of six smooth and six coarsened faces with curvature for each dodecahedron.

The curvature of rough faces was identified using atomic force microscopy (AFM) observation for this sample (Figure 1c). As far as can be observed, all the
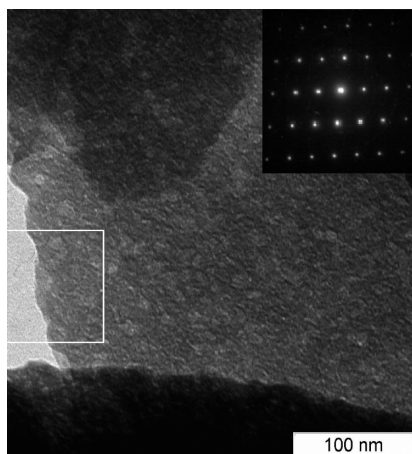
Figure 2. TEM images of a thin section and (inset) SAED pattern taken from the framed ultrathin section obtained from calcite pseudo-dodecahedral particles. [PSS-*co*-MA] = 0.1 g/L, [CaCl$_2$] = 1.25 mM, 2 weeks.

curved faces show a nanogranular surface structure with particles of about 150 nm in size (see also Supporting Information Figure S1). We formally ascribe the crystallographic planes of the six rough faces to the {011} family although they are curved and thus no crystal faces in the classical sense, whereas the other six smooth faces could be indexed to the {104} family.[36] To substantiate the indexing, we utilized the *Cerius*^{2} software to access the pseudo-dodecahedral morphology. The resulting model with {104} and {011} indices matches the as-obtained pseudododecahedra very well.[34] The existence of a 3-fold symmetry along the *c*-axis direction is also confirmed by the model. The XRD pattern[34] and FT-IR spectrum verified that the pseudo-dodecahedral product is pure calcite phase, as shown in Supporting Information Figure S2a. The sharp peaks of the XRD pattern of the dodecahedral product are very similar to those of the default calcite single crystals, suggesting that the dodecahedra are single crystals.[34] In the FTIR in Supporting Information Figure S2a, the non-

splitting peaks at 712 and 872 cm^{-1} correspond to the out-of-plane bending (υ_2) and the in-plane bending (υ_4) modes of the carbonate groups in calcite as already published in the literature.[37,38] The result supports that the CC composition in the sample is in the crystallographic form of the calcite phase.

The transmission electron microscopy (TEM) image (Figure 2) taken from an ultrathin section of the ultramicrotomed sample shows that these particles possess a large number of interstices with a length ranging from 2 to 10 nm and with porous architectures in the bulk. The interstices show the character of a nanoparticle-based crystallization pathway[26−29] although no separate nanoparticles can be observed anymore in the interior of the crystal in contrast to the nanogranular {011} surfaces observed by AFM (Figure 1 and Figure S1) and SEM. The selected area electron diffraction (SAED) taken from the framed area of the ultrathin section, as shown in the inset of Figure 2, enabled us to determine the single-crystalline nature of each dodecahedral calcite particle in agreement with XRD data.[34] This indicates that the single crystal was formed *via* a mesocrystal intermediate with subsequent Ostwald ripening of the flat {104} low energy faces, whereas the pseudo-{011} faces still show the nanogranular mesocrystal surface. Thermogravimetric analysis of this sample shows a content of *ca.* 2.0 wt % organic matter, which indicates the existence of incorporated polyelectrolyte molecules between boundaries of nanocrystallite domains.

Calcite single crystals with pseudo-dodecahedra morphologies were already literature reported with an amazing variety of additives, such as Mg^{2+},[39−41] Co^{2+},[42] simple organic acid,[35] phosphate,[35] carboxylate-rich polymers,[43] amino acids,[44] calcite-binding helical peptide,[45] lysozyme,[46] globular proteins,[47] and protein extracts isolated from aragonitic abalone shell nacre[48] and sea urchins.[49,50] The universal paradigm in these studies mainly relies on the selective adsorption of additives on the expressed faces,[49,51] the inhibiting effect of additives on the step-growth,[40] or the combination of the two mechanisms.[52] The influence of the organic matrix in determining the orientation and morphology of nanocrystallite aggregates, however, had never been investigated in these studies. Recently, aggregation was put forward as a general feature of crystallization at high supersaturation.[33,36,53−55] For example, calcite forms pseudo-octahedral mesocrystals when growing in polyacrylamide hydrogel networks.[53] The physical diffusion limitation in gels is the key to the ordered organization of rhombohedral building units. For our particles, the curved appearance, the absence of step-growth evidence, and the pores in the TEM thin cut also indicate a nonclassical crystallization pathway. This nonclassical crystallization pathway *via* mesocrystals involving elements of liquid minimum surface organization could indeed
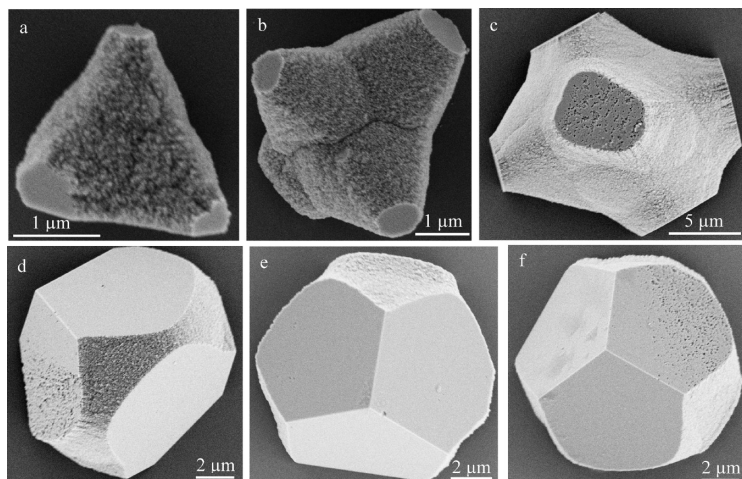

Figure 3. Calcite particles showing the curved surfaces. (a−c) the rhombohedral P-surface shape, (d) the transition shape, and (e, f) the pseudo-dodecahedral shape. [PSS-*co*-MA] = 0.0025 g/L, [CaCl$_2$] = 1.25 mM, in 1 week.

be evidenced by looking at the intermediates in a time-resolved study.[34]

To gain more insight into the formation of calcite pseudo-dodecahedral single crystals, the product obtained at a much lower PSS-*co*-MA concentration (0.0025 g/L) but the same CaCl$_2$ concentration (1.25 mM) was characterized by SEM. As shown in Figure 3, the intermediates obtained after 1 week are microparticles with different shapes. While only a small minority of the crystals transformed to display pseudo-dodecahedral morphology, the majority just evolved to show morphologies with the rhombohedral {104} faces but simultaneously displaying the curved minimum P-surfaces which are characteristic for a liquid and which were already found as early intermediates in the time-resolved study of dodecahedra formation.[34] These P-surface particles are smaller in size compared with those obtained at higher PSS-*co*-MA concentration but show the same morphogenesis sequence.

Comparative Morphogenesis by Face Selective Polymer Adsorption onto Seeds. Nucleation is a very important step in controlling the precipitation reaction. It directly influences the final particle shape and size and can even decide the whole growth mechanism. Indeed, the shape evolution of crystals grown in solution has been extensively discussed in mineralogy. Generally, the polymorph formation is determined by nucleation although indications exist that the polymorph is already encoded in prenucleation clusters even in undersaturated solutions.[56] However, the isotropic transformation often involves dissolution.[57] Here, both the single crystalline structure and the smooth {104} faces of the pseudo-dodecahedral particles could suggest that the unusual morphology could be formed by {011} face selective polymer adsorption to calcite rhombohedral particles which are formed by nucleation at the initial stage. This would be in agreement with dodecahedra formed in presence of malonic acid.[35] To address this question, we attempted to evoke shape control by face selective polymer adsorption after introducing foreign seeds at the start. The seed for the shape conversion process was chosen to be rhombohedral calcite particles prepared from 1.25 mM CaCl$_2$ by the gas-diffusion method. When PSS-*co*-MA of 0.1 g/L was used as the solution medium for the morphogenesis, only slight truncation at edge sites was observed after 2 weeks indicating face selective etching of the polymer (Figure 4a). When the mixture of PSS-*co*-MA of 0.1 g/L and CaCl$_2$ of 1.25 mM was used, the resultant crystals became larger in size with time indicating particle growth (Figure 4b and 4c) and displayed sleek edges after 2 weeks. These edges were formed by face selective polymer adsorption while the {104} faces also show etching pits. (Figure 4d) through irreversible dissolution.[57] The two sets of experiments demonstrate that rhombohedral calcite single crystal seeds in a growth solution containing the polymer do not produce pseudo-dodecahedral mor-
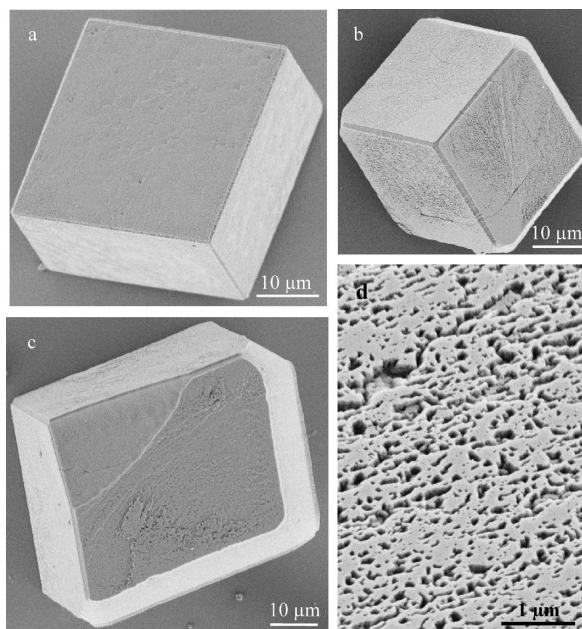

Figure 4. Dissolution and growth of calcite rhombohedral seeds in aqueous solutions by gas diffusion method (a) over 2 weeks in PSS-*co*-MA solution (0.1 g/L), (b) after 1 week in the mixture of CaCl$_2$ solution (1.25 mM) and PSS-*co*-MA (0.1 g/L), and (c) after 2 weeks in the mixture solution of CaCl$_2$ (1.25 mM) and PSS-*co*-MA (0.1 g/L); (d) SEM image of the (104) surface in panel c, showing the etching pits.

phology but a rhombohedron with truncated edges due to face selective polymer adsorption in a classical growth process. This is another indication for the non-classical crystallization pathway to pseudododecahedra.

Calcite Mesocrystalline Intermediates. At a PSS-*co*-MA concentration of 0.1 g/L, an abrupt transition in morphology was observed with increasing [Ca^{2+}] from 1.25 to 5 mM. In contrast to the pseudo-dodecahedral shape of calcite particles obtained at 1.25 mM, pseudo-octahedral shaped particles (Figure 5g) were observed for a [Ca^{2+}] concentration of 5 mM. The XRD pattern[34] and FT-IR spectrum (Figure S2b) confirmed the assignment of the product to a pure calcite phase. Examination of the primary particle size by a XRD peak broadening-based simulation suggests a primary nanoparticle size of 60−70 nm.[34] The direct observation of nanoparticles (Figure 5a) as precursor and P-surface intermediates with curved surfaces (Figure 5b,c) by SEM is helpful for providing structural insight into the growth of calcite pseudo-octahedral particles. The liquidlike appearance is obvious (Figure 5b−e). Figure 5f shows the typical SEM image of particles obtained after 1 week. These particles exhibit rough and scalloped surfaces and appear as ∼40 μm individual pseudo-octahedral microparticles with smooth {104} faces. Although angles and edges on a larger scale are well shaped, it is obvious that most of the exposed faces do not belong to the natural faces of calcite, but are assembled from oriented subunits. A 3-fold symmetry is
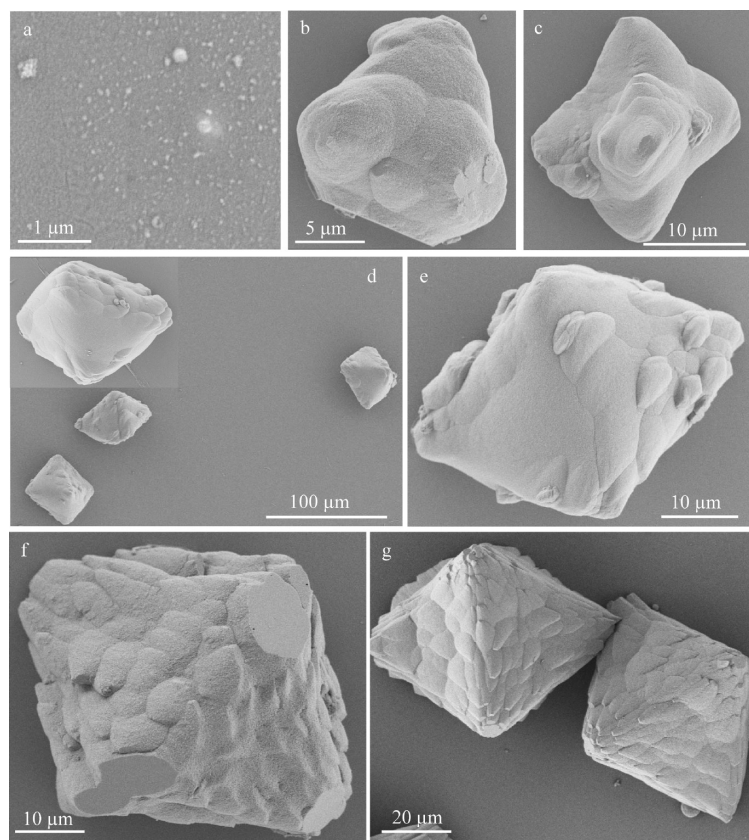
Figure 5. SEM image of precursor, intermediates, and calcite pseudo-octahedral particles grown for 5 h (a), 3 d (b), 4 d (c), 5 d (d, e) and the inset in panel d, 1 week (f), and 2 weeks (g). [PSS-*co*-MA] = 0.1 g/L, [CaCl₂] = 5 mM. In panel f the smooth faces (six apexes of the truncated octahedron) are ascribed to the {104} family.

evident through the two opposite equilateral triangular facets per octahedral particle. We attribute these two facets to (001) and (00$\bar{1}$), as indicated by the absence of birefringence under crossed polarizers.[36,50,58] The other remaining lateral triangular facets can not be constructed by simply connecting the end points of the two {001} triangles. Using faces of the {011} family for this interconnection would result in trigonally deformed {011} faces, which differ well beyond experimental error from the experimentally observed equilateral triangles.[34] Thus, a real octahedron cannot be constructed from a calcite single crystal. TEM was employed to observe the microstructure of the calcite pseudo-octahedral particles. TEM and high resolution TEM (HR-TEM) images of an ultrathin section of the obtained octahedral calcite mesocrystals show that the sample has a mesoporous structure.[34] Mesopores and defects under preservation of a joint crystal orientation are important characteristics of a mesocrystal, which originates from the interstitial voids of primary nanoparticle stacks within the whole aggregates.[26−33] Selected area electron diffraction (SAED) of this area shows a single-crystal diffraction pattern with minor distortions.[34]

Comparable observations were reported for fluoroapatite seed crystals grown in a gelatin gel[13,15] and for truncated triangular calcite mesocrystals,[30,31] suggest-

ing that a mesoscale transformation process occurs in the formation of these octahedral calcite aggregates. In other words, these are not single crystals, but energy minimized superstructures of nanocrystals. Note that both the texture and size of the octahedral calcite microparticles are different from pseudo-octahedral calcite mesocrystals constructed by rhombohedral building units in a specifically high supersaturation reaction environment relying on the limited diffusion in polyacrylamide gels.[36,53,59] The mesocrystals synthesized in aqueous solution in the presence of PSS-*co*-MA show faceted {104} faces characteristic of a single crystal as well as curvature indicative of liquid character (Figure 5f).

In addition, the obtained octahedral calcite has a BET surface area of 64.8 m² g⁻¹, which is much larger than a BET surface area (1.8 m² g⁻¹) of rhombohedral calcite grown in the absence of polymer. An unavoidable result that features the aggregation of nanocrystalline calcite subunits is the large occlusion of polymer molecules in the structure. Thermal gravimetric analysis (TGA, not shown) proved that a content of *ca*. 4.0 wt % polymer remained in the final product. The polymer content is only half as high (2.0 wt %) in the case of pseudododecahedra, underlining that those are the low polymer concentration species.

Indeed, the product structure and morphology has a significant dependence on both calcium and PSS-*co*-MA concentrations. A series of experiments was performed to investigate the effects of the calcium ion concentration at rather lower PSS-*co*-MA concentrations. For example, at a PSS-*co*-MA concentration of 0.0025 g/L, a morphological variation from pseudo-dodecahedral to pseudo-octahedral was also observed when Ca concentration was increased from 1.25 to 5−20 mM. This means that the structural transition from single crystal to mesocrystal is already triggered by the smallest concentrations of polyelectrolyte.

Figure 6 shows the growth evolution of the particles. It is interesting to note that the initial nanoparticle aggregates formed already after 30 h (Figure 6a). When the reaction time was increased to 2 d, scaffolded embryos contoured with the differentiated octahedral shape resulted (Figure 6b). When the reaction time was further increased to 4 d, the particles grew further with nearly completed octahedral shapes (Figure 6c,d). At this stage, the octahedral particles are uniform and of a high yield. Each octahedron consists of six smooth faces and two coarse faces. As shown in the high resolution SEM image (Figure 6e), the roughened faces expose many smaller and highly aligned subunits, thus clearly displaying mesocrystal features. The roughening is on the order of 100 nm (Figure 6i), and the undulation of the surface structure is observable (Figure 6j).

Looking more carefully onto the particles, it is easy to find that every roughened face is an equilateral triangle plane with interplanar angles of 60°. A 3-fold symmetry exists through the centers of two such roughened faces per crystal. The construction toward well-defined octahedral shapes approached completion after 6 d. AFM characterization provides considerable insight into the textures of the intermediate particles. Although the further growth generated round tips and made the difference between the smooth and coarse faces disappear in the SEM experiment (Figure 6f), it still proves the presence of mesocrystals with respect to the appearance of rugged and scalloped faces texture and the observation of smaller building units on their surfaces.

Interestingly, the particles obtained after 6 d exhibited two types of mechanical behavior of their surfaces, as demonstrated in the phase contrast mode of AFM, shown in Figure 6k,l. One type of face is severely biphasic, the other is homogeneous. It indicates that there are two groups of faces with different crystal plane characteristics in each particle. We ascribe the crystallographic planes of the roughened and biphasic faces in the intermediate particles to the (001) and (00$\bar{1}$) faces, respectively. The basal planes of the {001} family consist of alternate layers of Ca ions and carbonate, thus creating a dipolar surface, which is a high energy face (see Supporting Information Figure S3). The relative surface energies for calcite faces are 0.7064 (104) and 2.4872 (001) J/m^2.[42,60] Such surfaces favor the trapping of charged polymers by Coulomb interactions. The interaction conversely stabilizes the (001) and (00$\bar{1}$) faces and lowers their surface energy. Therefore the biphasic soft–hard character of these faces is plausible.

To verify the structural features of the calcite octahedral mesocrystals, we microtomed the particles shown in Figure 6f and characterized the ultrathin slices by TEM. A 3D alignment of nanoparticles with high orientation was found over multiple length scales, as shown in Figure 7. Although some individual nanoparticles within a local area seem to be random, the overall crystalline aggregates exhibit long-range ordering of the elemental nanocrystallites. This provides an evidence to
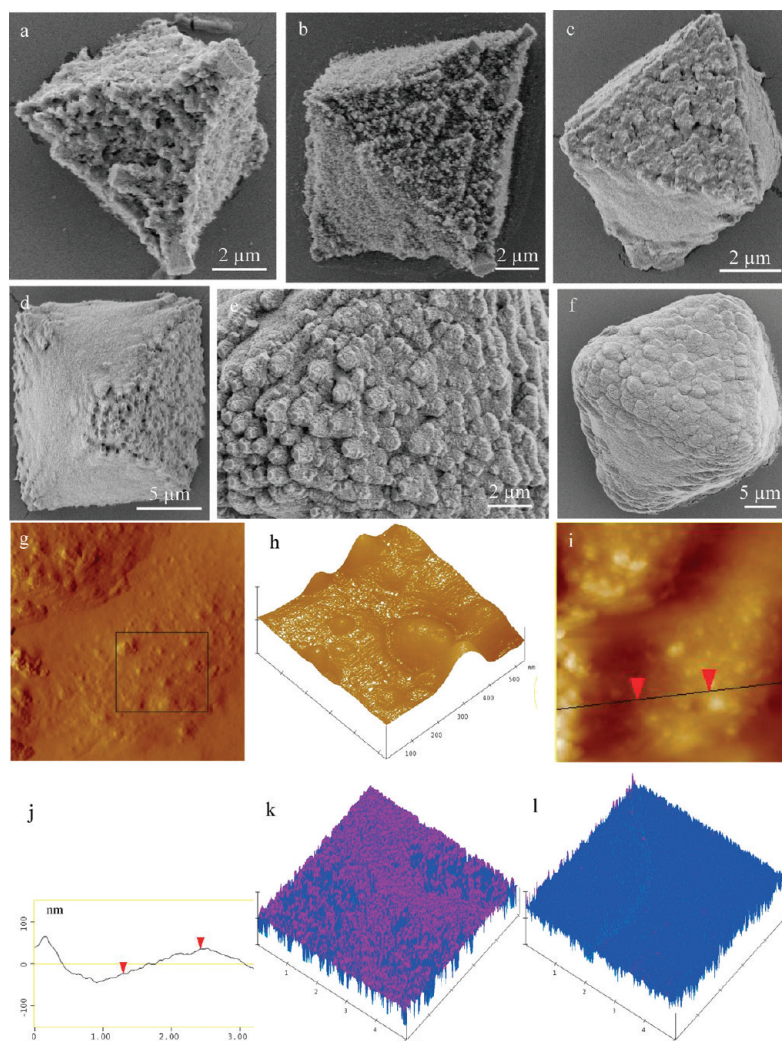

Figure 6. Calcite mesocrystals and the intermediates obtained by time-resolved experiments. [PSS-*co*-MA] = 0.0025 g/L, [CaCl$_2$] = 20 mM. SEM images of products obtained after 30 h (a), 2 d (b), 4 d (c−e), and 6 d (f). (g) AFM height image (3 μm × 3 μm), (h) 3D rough image of the area framed by black lines in panel g and (i, j) section height analysis, showing the rugged face appearance; (k) biphased and (l) homogeneous AFM phase images taken from crystal faces. The crystal morphology is shown in Figure 6f.
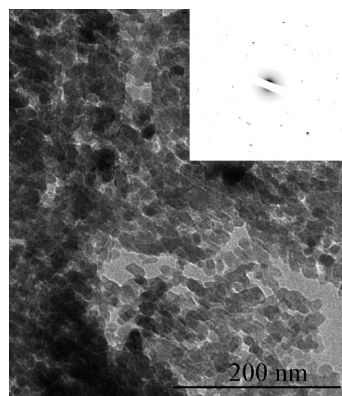

Figure 7. TEM image showing the oriented alignment of nanocrystallites. It was taken from an ultrathin section of calcite octahedral mesocrystals shown in Figure 6f. The corresponding SAED pattern is in the inset. [PSS-*co*-MA] = 0.0025 g/L, [CaCl$_2$] = 20 mM, 6 d.
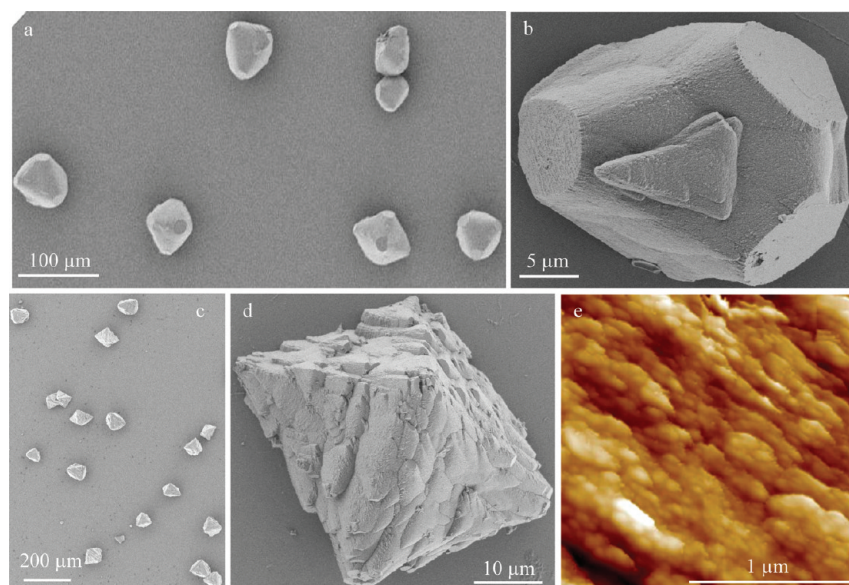
Figure 8. SEM images of intermediate particles obtained after 4 d (a, b) and 2 weeks (c, d). (e) AFM image showing the highly oriented location of nanoparticles on the crystal faces. [PSS-*co*-MA] = 1.0 g/L, [CaCl$_2$] = 2 mM.

assign nanoparticle-mediated aggregation as the crystallization mechanism.

Intermediates with rhombohedral P-surface morphologies were obtained after 4 d at [PSS-*co*-MA] = 1 g/L and [Ca] = 2 mM. SEM images of the particles are shown in Figure 8a,b. From the rough concave faces, it can be clearly seen that the particles are formed by nanoparticles. The six flat faces per particle can again be assigned to the {104} family. Here, both the features of nanoparticle aggregation as well as the P-surface morphologies of the superstructure bear strong resemblance with the intermediates of dodecahedral particles. But the intermediate particles have a size twice of that in the case of dodecahedral particles (Figure 3a–c). In addition, some particles carry smaller P-surface embryos on their curved faces (Figure 8b). These results suggest the occurrence of multiple particle generations during the growth process and aspects of self-similarity in the organizing joint crystal field.[32,61] From the fact that in the final sample the smaller intermediates have vanished (Figure 8c), the presence of dissolution and recrystallization or (more likely) joint attachment to the parental bigger microparticle under partial reorganization of their structure has to be deduced. This could explain the scalloped structure of six of the eight faces in each octahedron (see Figures 5f,g and 6f).

The morphology of the particles further changes with crystallization time. As found for lower [PSS-*co*-MA] concentrations already at shorter times, the intermediary P-surface ripened to pseudo-octahedra when the growth time was extended to 2 weeks. Figure 8 panels c and d show SEM images of the sample obtained after 2 weeks in the presence of [PSS-*co*-MA] =

1 g/L and [Ca] = 2 mM. Figure 8c is a typical SEM image with low resolution. The sample contains abundant octahedra (Figure 8d) with edge lengths of approximately 30–40 μm. Figure 8e shows the typical AFM image of one octahedron surface. Again, AFM shows the granular character very well across the whole pseudoface. The nanoparticles are easily seen, with a mean diameter of ~100 nm. Both SEM and AFM images show the absence of the classical step growth mechanism, but a large number of nanoparticles on the surfaces of the mesocrystalline arrays.

Calcite Polycrystalline Particles. In the last set of experiments, the crystallization was conducted in the presence of PSS-*co*-MA and Ca both of higher concentrations. Increasing [Ca^{2+}] by the factor of 4 and maintaining [PSS-co-MA] at 1 g/L gave well-defined polycrystalline calcite spheres with diameters in the range of 30–55 μm (Figure 9a), instead of the pseudo-octahedral mesocrystals obtained at [Ca] = 2 mM. The spheres are highly uniform in size. The calcite phase of the product was confirmed by XRD pattern (Supporting Information Figure S4).

A continuous change in morphology and crystallographic phase was observed with the variation of [PSS-*co*-MA] at constant [Ca^{2+}]. For instance, flat and hollow ellipsoidal hemispherical and spherical particles with diameter of 4–6 μm (Figure 9b,c) were obtained after 3 d at [PSS-*co*-MA] = 0.025 g/L and [Ca] = 20 mM, while maintaining the concentration of Ca at 20 mM but increasing the concentration of PSS-*co*-MA by a factor of 4 yields hollow spheres with an mean diameter of 7–8 μm after 3 d (Figure 9d–f). A core–shell assembly structure with a shell thickness of 40 nm can be observed by the SEM image of the product at this stage (Figure 9e). The external layer on the inner core is constituted of visible nanocrystallites. The shells of the multiply layered spheres are mechanically not stable and can be peeled off from the cores by external forces (Figure 9e). Further increasing the concentration of PSS-*co*-MA to 0.05–1 g/L gives hollow spherules with an inside diameter of 10 μm and outside diameter of 50–90 μm after 3 d (Figure 9g). The radial alignment of nanocrystallites in the wall of the bigger hollow spheres can be clearly seen from SEM images of the crushed sample (Figure 9h). As evidenced by FT-IR analysis (Figure S2) and XRD measurement (Figure S4), there is a phase transformation from vaterite (Figure 9b,c) through a mixture of vaterite and calcite (Figure 9d–f) to calcite (Figure 9g,h).

Particle Formation and Morphogenesis. Time-resolved experiments provide important evidence to identify the

underlying mechanisms and further elucidate the relationships among the as-synthesized crystals. An important point decisive for the further fate of morphogenesis is the capture and stabilization of ACC nanoparticles at the early stage of the crystallization process.[34] This can be attributed to the nucleation inhibiting and nanoparticle stabilization effect of PSS-*co*-MA. Addadi and Weiner *et al*. suggested that biological macromolecules induce the formation of a transient ACC phase at early stages of growth, which transforms to calcite at a later stage in sea urchin larval spicules.[62,63] Amorphous phase synthetically produced in aqueous polymer and Ca^{2+} solution is, however, different from the biogenic transient ACC phase, as water would be inevitably incorporated into the phase while the biogenic transient ACC phases contain no water.[62,64] Titration measurements in analogy to those reported in ref 65 show that nucleation is largely delayed when PSS-*co*-MA instead of PSS was used as the additive in the crystallization process.[34] The result backs up the observation of ACC nanoparticles in the solution at early stage.

The finding that practically all generated particles are close-to-spherical (a crystalline shape generated from a close to spherical intermediate) and about monodisperse, with their size increasing both with mineral and polymer concentration reflects the next step of morphogenesis. Typically, spheres are formed from a fluid, here a nanoparticle aggregate with fluid character as we see the primary nanoparticles still at later stages. We assume that the primary amorphous particles precipitate from water into a joint liquid phase, in which the integration of PSS-*co*-MA[66] prevents the primary particles from tight, irreversible aggregation (Scheme 1 A1, A2, B1, and B2). Because of a high Hamaker constant of these ACC nanoparticles[67] and their critically high concentration, they exhibit a strong tendency for colloidal phase formation (Scheme 1 A2, B2) toward liquid droplets of nanoparticles, which are in addition about monodisperse. This mesoliquid is held together by the attractive van der Waals force between the individual nanoparticles. This liquidlike, colloidal phase has to be distinguished from polymer induced liquid precursor (PILP) phases, which are described as classical molecular liquids without recognizable substructure,[68−70] whereas nanoparticles are observed in the present case. The liquidlike character of those droplets is also derived from the formation of the intermediate particles with rhombohedral P-surface morphologies. Such minimal surfaces occur in cases where a surface tension controls the arrangement of two dissimilar liquids, such as lipid−water or surfactant−water mixture.[71]

The further fate of this hybrid phase of nanoparticles now depends on the specific reaction conditions. In the case of the pseudo-dodecahedra, nucleation of a calcite nanoparticle with six {104} faces (Scheme 1 A3) and with their subsequent growth by attachment and
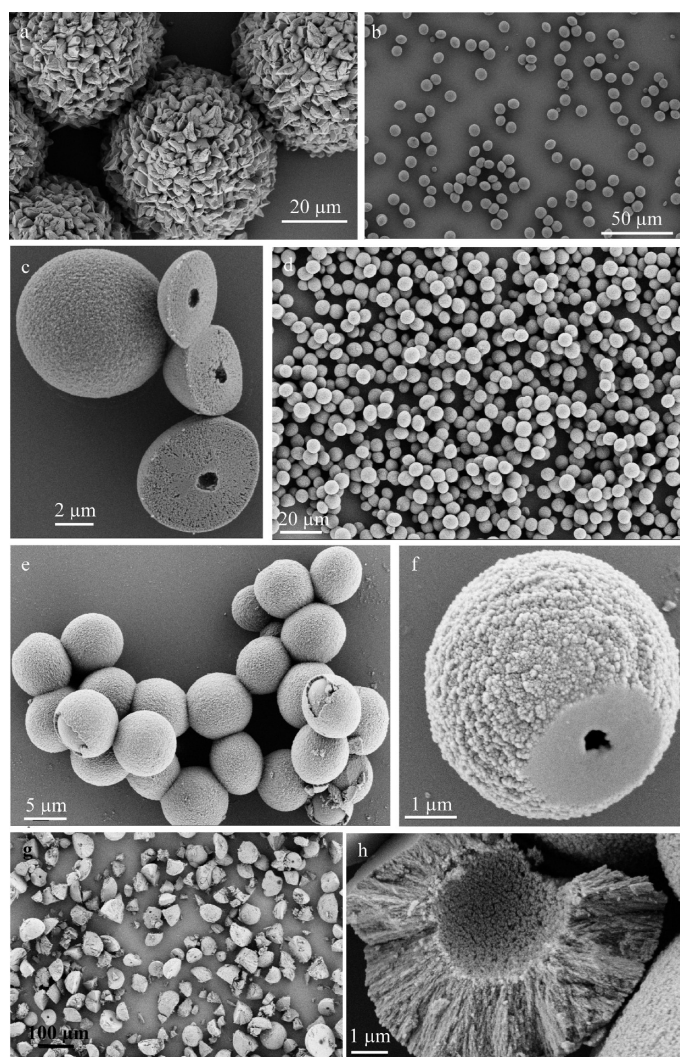

Figure 9. SEM images of the obtained calcite polycrystalline aggregates grown for 3 days. [CaCl₂] = 10 mM, [PSS-*co*-MA] = 1 g/L (a). [CaCl₂] = 20 mM (b−h). [PSS-*co*-MA] = 0.025 g/L (b,c), 0.01 g/L (d−f), 0.05−1 g/L (g, h). The particles in panels g and h were crushed.

crystallization of neighboring ACC nanoparticles leads to a skeleton composed of 3 rods with mutual angles corresponding to those between the {104} faces (Scheme 1 A4). A liquid being contained in such a droplet with a single crystalline skeleton inside would automatically deform into the P-surface shaped aggregates upon drying or shrinking or upon scaffold growth, which is strongly evidenced by the simultaneous presence of single crystal faces and nanotectons in one and the same object. This leads to the observed curved P-surfaces, which are controlled by the surface tension of the liquid (Scheme 1 A4 and B5).

In this product, the mesostructures share the features of a crystalline solid and a liquid crystal at the same time. The "hard", weakly polymer controlled crystallization directions define the directionality of the single crystal skeleton and edges, whereas the polymer stabilized, hydrated, "soft directions" originate from the joint character of the soft condensed precursor
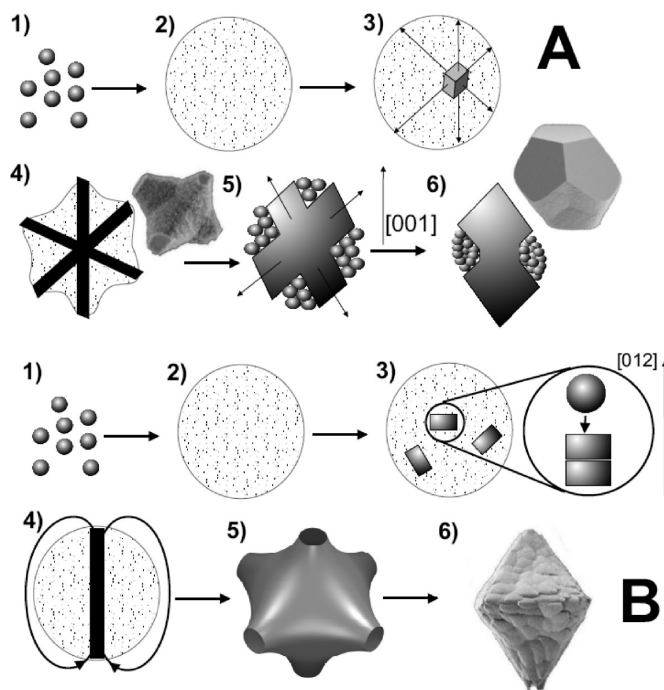
Scheme 1. Schematic illustration of the CaCO₃ crystallization in the presence of PSS-*co*-MA. (A) Dodecahedron formation: (1) formation of polyelectrolyte stabilized ACC nanoparticles; (2) aggregation of ACC nanoparticles to form liquidlike aggregates (the dots represent the ACC nanoparticles for clarity reasons); (3) calcite nanoparticle crystallization with six {104} faces; (4) growth along the six {104} faces and deformation of the liquid aggregate within the crystalline skeleton; (5, 6) Ostwald ripening of {104} and further growth fuses three {104} faces at both sides of the crystal leaving rough crystallized former P-surfaces in between forming the dodecahedra. (B) Growth of pseudo-octahdedral mesocrystals. (1, 2) As described above for the dodecahedra; (3) crystallization of calcite nanoparticles with one charged high energy face stabilized by the polyelectrolyte and further growth by oriented attachment of crystalline nanoparticles or ACC; (4) crystalline rods have a dipole field (shown only for one rod for clarity reasons). Minimization of interaction between dipole fields leads to three perpendicularly oriented rods with mutual 90° angles. (5) Deformation of the liquid aggregate along the crystalline skeleton leads to P-surface formation while patches of liquidlike ACC aggregates attach to the particle (not shown for clarity reasons); (6) further disposed patches of liquidlike phase crystallize without fusion to a single interface leading to the scalloped surface of the mesocrystal. For the sake of clarity, the polymer is not included into the drawing. Also, the three-dimensional structures are projected into two dimensions and supplemented by SEM images

and its surface tension. This enables the generation of rounded surfaces and the exposure of directions which cannot be attributed to the inherent crystal symmetry. If little polymer is present, the {104} faces on the tips can grow and Ostwald ripening and further growth fuses three neighboring {104} faces leaving the liquid aggregate in between (Scheme 1 A5 and A6). Depending on polymer concentration, these P-surface dominated assemblies can be stable for a rather long time, but when they crystallize, the nanoparticles get into crystallographic register and form a mesocrystal with P-surface shape forming the rough faces of the finally observed pseudo-dodecahedra in addition to the six smooth {104} faces. The curvature and inward bending is amplified by the 40% volume contraction upon calcite formation from the less dense ACC.

For the formation of the pseudo-octahedra, nucleation and oriented attachment of a crystalline scaffold within the droplets with their moderate mobility obviously results in a hexapod, the size and symmetry of which is exactly controlled by the size of the intermediary microdroplet and its surface tension (each arm can only grow until the surface of the droplet is reached; "poking" out would result in a stop of growth/disassembly again). This explains the about perfect preservation of the octahedral shape, although no "real faces" are involved. Similar multipods grown by additive directed crystal growth are well-known from heavy metal chalcogenides,[72] but are in contrast to our case encoded by crystal symmetry and grown by classical crystallization.

The direction of oriented attachment and axis of the primary rod is not easy to identify, as the clearly identifiable (104) caps are tilted toward the hexapod direction. Because two of the eight octahedral sites are aligned in *c*-direction, {012} is a meaningful option as this is a highly charged face like {001} which should be a good adsorption site for the applied polyanions (Figure S4). Owing to the symmetry of calcite, a dipolar character is not present in the crystal itself, but can be generated if polymers adsorb on only one of the charged faces.[30,31] This leads to dipolar nanoparticles which can aggregate along the [012] axis (Scheme 1 B2) or quite probably by oriented attachment of ACC nanoparticles as already evidenced for {001}.[30,73] A hexapod is the direct consequence of dipole repulsion between the single rods to be aligned: repulsion energy is minimal for three rods aligned in three different orthogonal directions as the three sets of p-orbitals (Scheme 1 B4 and B5). As in the case of pseudo-dodecahedra discussed before, the liquid aggregates will form P-surfaces around the crystalline skeleton which are controlled by the surface tension of the liquid (Scheme 1 B5). Further liquid aggregates attach to the P-surfaces, which can already be crystallized hindering a fusion of the liquid phases (Figure 7b) and thus forming a patched surface structure. This leads to the finally observed pseudo-octahedron after crystallization of the liquid aggregates (Scheme 1 B6).

For the final, high mineral and high polymer concentration product, the fluid in the droplets cannot form a skeleton by oriented attachment, and heterogeneous nucleation from the surface takes over: crystal balls and shells are formed. With the large increases in the concentrations of Ca and PSS-*co*-MA, the formation of nanocrystallites speeds up significantly. Growth from the surface while increasing the density of the material upon crystallization of ACC (40% volume decrease) inevitably results in the formation of hollow zones, which can be located between the layers or finally even in the core of the structure, resulting in "multilayer spheres" or hollow crystal balls, respectively. It is however again the existence of a highly concentrated colloidal mesofluid droplet driving overall structure forma-

tion, with the void volume giving a measure for the amount of solvent and volume shrinkage.

The loss of crystallization control due to too high thermodynamic driving forces is also reflected in a lost polymorph control. Rapid crystal nucleation usually gives rise to the formation of vaterite phase products, which later transform to calcite to attain a higher stability. Indeed, a temporal morphology transition of "hexagonal lenses" to "hollow spheres" to "multiple-layered hollow spheres" was observed. According to FT-IR analysis (Figure S2c), the sphere product obtained from a solution containing 20 mM Ca and 0.01 g/L PSS-*co*-MA after 3 d is a mixture of vaterite (1084 and 745 cm^{-1} characteristic peaks) and calcite (1394, 872, and 712 cm^{-1} characteristic peaks).[37,38,74] In agreement with the FTIR result, the hexagonal lens microstructures (Supporting Information Figure S5) obtained at the early stages are similar to the reported CC product with vaterite phase.[21]

Finally, the careful analysis of the surface structure within the faces of the mesocrystalline pseudo-octahedral assembly gives a remarkable insight on how the presence of the scaffold surface and the connected dipolar force fields influence the crystallization of the remaining (liquid) amorphous droplets. Figure 10 depicts a high magnification of one of the faces of a calcite octahedron directly after recrystallization. It is obvious that the single crystal skeleton does not extend through every patch of newly deposited material. Moreover, the structure is grown in a patch like fashion where the register of the crystallographic orientation is a reflection of the 3D alignment within the mesocrystal. In that way, the primary nanoparticles transform on the surface into small versions of the bigger mesocrystal, even exposing small {104} tips in the correct orientation on the surface of deposited particles.

SUMMARY AND CONCLUSIONS

Our ability to control nanoparticle aggregation through the use of random copolymer polyelectrolytes provides us with the chance to create a model system of controlled CaCO$_3$ crystallization which is remarkably rich in morphologies and elaborated a unifying crystallization scenario being able to explain the found structural complexity. Contrary to classical crystallization and nucleation and growth, the precipitation takes place under nonequilibrium conditions which are, however, highly defined.

As in many additive controlled crystallization reactions, molecular supersaturation is practically instantaneously lowered by the formation of amorphous nanoparticles. It is more peculiar for the present stabilizer that the stabilization of those nanoparticles is only intermediary so that the particles themselves aggregate to larger droplets of 10−100 μm size, however, preserving the fluid nanoparticle assembly character.

For all different observed morphologies, it is important what happens in the initially formed liquid aggre-
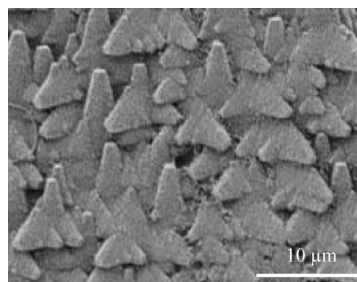

Figure 10. SEM of enlarged surface structure of calcite pseudo-octahedral mesocrystals, showing the alignment of small building units made up by nanoparticles; 6 days, [PSS-*co*-MA] = 1.0 g/L, [CaCl$_2$] = 2 mM.
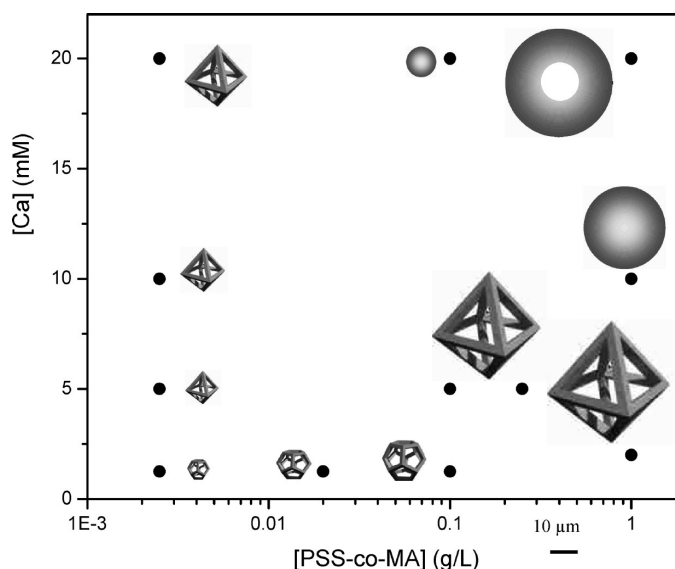

Figure 11. Morphology diagram for calcite obtained by the gas diffusion method in the presence of PSS-*co*-MA showing the morphology dependence on concentrations of Ca and polymer additive. The particles are drawn to scale. The animations of dodecahedral and octahedral can be found at http://www.3quarks.com/GIF-Animations/PlatonicSolids. The *x* axis is presented at logarithm scale.

gate of ACC nanoparticles. The fate of the initial liquid aggregate is highly controlled by the polymer concentration as well as that of calcium. Slow crystallization at low [Ca^{2+}] concentrations leads to formation of the rhombohedral calcite nanoparticle seeds which will then extend to rods on the {104} faces and lead to scaffold forming rhombohedral P-surfaces (Figure 3c) and finally the pseudo-dodecahedra. At higher [Ca^{2+}] concentrations, a hexapod is formed by three rods exhibiting dipole fields and thus orient with mutual 90° angles due to dipole repulsion, again being a skeleton for the formation of P-surfaces of the liquid aggregate controlled by surface tension. This leads to the pseudo-octahedral particles, as a higher driving force toward crystallization can also lead to nonequilibrium morphologies of the primary nanocrystals,[75] which can explain the generation and subsequent polymer stabilization of the high energy {012} or similar faces. Finally at the highest [Ca^{2+}] concentrations and also highest polymer addi-

tive concentrations, surface nucleation on the liquid aggregate phase gets favored over nucleation inside this phase resulting in multilayered and hollow spheres.

Such an easily attainable method overcomes limitations of traditional crystal engineering strategies, as it requires no changes in reaction temperature, chemical components, or solvent but allows for a variety of morphologies available at ambient conditions by simple variation of reactant concentrations. As shown in Figure 11, we categorize the as-obtained calcite microstructures in the morphology diagram into three classes according to their morphological and structural features, that is, mesocrystals with large single crystalline parts[76] (pseudo-dodecahedra), mesocrystals with single crystalline skeleton (pseudo-octahedra), and polycrystalline spherical aggregates.

More specifically, the finding of scaffold structure formation by oriented assembly and its effect on exerting oriented assembly and crystallization in a collective force field may have significant impacts on the fundamental understanding of the observation of naturally formed biomineral structures exposing minimal surfaces, such as sea urchins, and the design of novel biomimetic materials. The versatile crystallization protocol offers effective means to the precise design and control over nanoparticle assembly which holds promise for extension to other materials with their performance depending on the shape and structure.

METHODS

Materials. All chemicals, calcium chloride, and ammonium carbonate (Aldrich), poly(4-styrenesulfonate-*co*-maleic acid) (PSS-*co*-MA) (sodium salt, 25 wt % in water, obtained from Aldrich, average molecular weight = 20 000, styrene/maleic acid molar ratio = 3:1) were of analytical grade and were used without further purification. All glassware (glass bottle and small pieces of glass substrate) was cleaned and sonicated in ethanol for 5 min, rinsed with distilled water before being further soaked with a H_2O-HNO_3 (65%)$-H_2O_2$ (1:1:1,V/V/V) solution, then rinsed with doubly distilled water, and finally dried in air with acetone.

Synthesis. The crystallization of $CaCO_3$ was carried out in a closed desiccator at room temperature (22 ± 3 °C). In a typical run, a solution (A) of $CaCl_2$ (20 mM) and a mixture solution (B) containing 0.25 mM polymer and 20 mM $CaCl_2$ were prepared by using doubly distilled water freshly bubbled with nitrogen overnight. After 9.8 mL of solution A and 0.2 mL of solution B were injected into a glass bottle (30 mL) with glass slides under stirring, the bottle was covered with parafilm, punched with three holes, and placed in a closed desiccator at room temperature. One glass beaker (50 mL) with crushed ammonium carbonate powder was also covered with parafilm, punched with three needle holes, and put at the bottom of the desiccator in advance. After different periods of time, the crystals were recovered, briefly washed with water, and allowed to dry. After gold coating, the crystals were examined with a scanning electron microscope. The time dependent crystallization experiments were done by taking out the small pieces of glass slides from the bottles in order to stop the reaction for examination.

Charaterization. Powder X-ray diffraction (XRD) patterns were recorded on a PDS 120 diffractometer (Nonius GmbH, Solingen) with Cu Kα radiation (λ = 1.542 Å). Thermogravimetric analysis was carried out under a stream of nitrogen, at a heating rate of 10 °C/min using a Netzsch TGA-209. N_2 adsorption measurements were performed at 77 K using a Micromeritics ASAP 2010 system utilizing Barrett−Emmett−Teller (BET) calculations for surface area and Barrett−Joyner−Halenda (BJH) calculations for pore size distribution for the adsorption branch of the isotherm. The SEM measurements were performed on a LEO 1550, GEMINI microscope. TEM, HRTEM images, and SAED were obtained on a JEOL-2010 microscope operated at 200 kV. The samples were embedded in epoxy resin and ultramicrotomed for the TEM measurements. The surface cleavage of the crystal faces, the unit cell structure, and the modeling of morphology were performed with the *Cerius*[2] software (Accelrys). The AFM images were obtained by means of a Digital Instruments nanoscope IIIa Multimode AFM (Digital Instruments Inc., Santa Barbara, CA).

Supporting Information Available: Figures S1, S2, S3, S4, S5. The material is available free of charge *via* the Internet at http://pubs.acs.org.

REFERENCES AND NOTES

1. Alivisatos, A. P. Biomineralization-Naturally Aligned Nanocrystals. *Science* **2000**, *289*, 736–737.
2. Pacholski, C.; Kornowski, A.; Weller, H. Self-Assembly of ZnO: From Nanodots, to Nanorods. *Angew. Chem., Int. Ed.* **2002**, *41*, 1188–1191.
3. Yin, Y.; Alivisatos, A. P. Colloidal Nanocrystal Synthesis and the Organic−Inorganic Interface. *Nature* **2005**, *437*, 664–670.
4. Zhang, Z. L.; Glotzer, S. C. Self-Assembly of Patchy Particles. *Nano Lett.* **2004**, *4*, 1407–1413.
5. Zhang, Z. P.; Sun, H. P.; Shao, X. Q.; Li, D. F.; Yu, H. D.; Han, M. Y. Three-Dimensionally Oriented Aggregation of a Few Hundred Nanoparticles into Monocrystalline Architectures. *Adv. Mater.* **2005**, *17*, 42–47.
6. Shevchenko, E. V.; Talapin, D. V.; Kotov, N. A.; O'Brien, S.; Murray, C. B. Structural Diversity in Binary Nanoparticle Superlattices. *Nature* **2006**, *439*, 55–59.
7. Urban, J. J.; Talapin, D. V.; Shevchenko, E. V.; Kagan, C. R.; Murray, C. B. Synergismin Binary Nanocrystal Superlattices Leads to Enhanced P-Type Conductivity in Self-Assembled PbTe/Ag_2Te Thin Films. *Nat. Mater.* **2007**, *6*, 115–121.
8. Banfield, J. F.; Welch, S. A.; Zhang, H. Z.; Ebert, T. T.; Penn, R. L. Aggregation-Based Crystal Growth and Microstructure Development in Natural Iron Oxyhydroxide Biomineralization Products. *Science* **2000**, *289*, 751–754.
9. Li, Z.; Chung, S. W.; Nam, J. M.; Ginger, D. S.; Mirkin, C. A. Living Templates for the Merarchical Assembly of Gold Nanoparticles. *Angew. Chem., Int. Ed.* **2003**, *42*, 2306–2309.
10. Penn, R. L.; Banfield, J. F. Imperfect Oriented Attachment: Dislocation Generation in Defect-Free Nanocrystals. *Science* **1998**, *281*, 969–971.
11. Tang, Z. Y.; Kotov, N. A. One-Dimensional Assemblies of Nanoparticles: Preparation, Properties, and Promise. *Adv. Mater.* **2005**, *17*, 951–962.
12. Tang, Z. Y.; Zhang, Z. L.; Wang, Y.; Glotzer, S. C.; Kotov, N. A. Self-Assembly of CdTe Nanocrystals into Free-Floating Sheets. *Science* **2006**, *314*, 274–278.
13. Busch, S.; Dolhaine, H.; DuChesne, A.; Heinz, S.; Hochrein, O.; Laeri, F.; Podebrad, O.; Vietze, U.; Weiland, T.; Kniep, R. Biomimetic Morphogenesis of Fluorapatite-Gelatin Composites: Fractal Growth, the Question of Intrinsic Electric Fields, Core/Shell Assemblies, Hollow Spheres and Reorganization of Denatured Collagen. *Eur. J. Inorg. Chem.* **1999**, *10*, 1643–1653.

14. Kawska, A.; Hochrein, O.; Brickmann, A.; Kniep, R.; Zahn, D. The Nucleation Mechanism of Fluorapatite—Collagen Composites: Ion Association and Motif Control by Collagen Proteins. *Angew. Chem., Int. Ed.* **2008**, *47*, 4982–4985.

15. Kniep, R.; Busch, S. Biomimetic Growth and Self-Assembly of Fluorapatite Aggregates by Diffusion into Denatured Collagen Matrices. *Angew. Chem., Int. Ed.* **1996**, *35*, 2624–2626.

16. Simon, P.; Zahn, D.; Lichte, H.; Kniep, M. Intrinsic Electric Dipole Fields and the Induction of Hierarchical form Developments in Fluorapatite-Gelatine Nanocomposites: A General Principle for Morphogenesis of Biominerals. *Angew. Chem., Int. Ed.* **2006**, *45*, 1911–1915.

17. Balz, M.; Therese, H. A.; Li, J. X.; Gutmann, J. S.; Kappl, M.; Nasdala, L.; Hofmeister, W.; Butt, H. J.; Tremel, W. Crystallization of Vaterite Nanowires by the Cooperative Interaction of Tailor-Made Nucleation Surfaces and Polyelectrolytes. *Adv. Func. Mater.* **2005**, *15*, 683–688.

18. Chen, S. F.; Yu, S. H.; Jiang, J.; Li, F. Q.; Liu, Y. K. Polymorph Discrimination of CaCO₃ Mineral in an Ethanol/Water Solution: Formation of Complex Vaterite Superstructures and Aragonite Rods. *Chem. Mater.* **2006**, *18*, 115–122.

19. Cölfen, H.; Antonietti, M. Crystal Design of Calcium Carbonate Microparticles Using Double-Hydrophilic Block Copolymers. *Langmuir* **1998**, *14*, 582–589.

20. Cölfen, H.; Qi, L. M. A Systematic Examination of the Morphogenesis of Calcium Carbonate in the Presence of a Double-Hydrophilic Block Copolymer. *Chem.—Eur. J.* **2001**, *7*, 106–116.

21. Gao, Y. X.; Yu, S. H.; Cong, H. P.; Jiang, J.; Xu, A. W.; Dong, W. F.; Cölfen, H. Block-Copolymer-Controlled Growth of CaCO₃ Microrings. *J. Phys. Chem. B* **2006**, *110*, 6432–6436.

22. Qi, L. M.; Li, J.; Ma, J. M. Biomimetic Morphogenesis of Calcium Carbonate in Mixed Solutions of Surfactants and Double-Hydrophilic Block Copolymers. *Adv. Mater.* **2002**, *14*, 300–303.

23. Rudloff, J.; Antonietti, M.; Cölfen, H.; Pretula, J.; Kaluzynski, K.; Penczek, S. Double-Hydrophilic Block Copolymers with Monophosphate Ester Moieties as Crystal Growth Modifiers of CaCO₃. *Macromol. Chem. Phys.* **2002**, *203*, 627–635.

24. Yu, S. H.; Cölfen, H.; Antonietti, M. Polymer-Controlled Morphosynthesis and Mineralization of Metal Carbonate Superstructures. *J. Phys. Chem. B* **2003**, *107*, 7396–7405.

25. Yu, S. H.; Cölfen, H.; Hartmann, J.; Antonietti, M. Biomimetic Crystallization of Calcium Carbonate Spherules with Controlled Surface Structures and Sizes by Double-Hydrophilic Block Copolymers. *Adv. Funct. Mater.* **2002**, *12*, 541–545.

26. Cölfen, H.; Antonietti, M. Mesocrystals: Inorganic Superstructures Made by Highly Parallel Crystallization and Controlled Alignment. *Angew. Chem., Int. Ed.* **2005**, *44*, 5576–5591.

27. Cölfen, H.; Mann, S. Higher-Order Organization by Mesoscale Self-Assembly and Transformation of Hybrid Nanostructures. *Angew. Chem., Int. Ed.* **2003**, *42*, 2350–2365.

28. Helmut Cölfen, M. A. *Mesocrystals and Nonclassical Crystallization*; Wiley: New York, 2008.

29. Niederberger, M.; Cölfen, H. Oriented Attachment and Mesocrystals: Non-Classical Crystallization Mechanisms Based on Nanoparticle Assembly. *Phys. Chem. Chem. Phys.* **2006**, *8*, 3271–3287.

30. Wang, T. P.; Antonietti, M.; Cölfen, H. Calcite Mesocrystals: "Morphing" Crystals by a Polyelectrolyte. *Chem.—Eur. J.* **2006**, *12*, 5722–5730.

31. Wang, T. X.; Cölfen, H.; Antonietti, M. Nonclassical Crystallization: Mesocrystals and Morphology Change of CaCO₃ Crystals in the Presence of a Polyelectrolyte Additive. *J. Am. Chem. Soc.* **2005**, *127*, 3246–3247.

32. Xu, A. W.; Antonietti, M.; Yu, S. H.; Cölfen, H. Polymer-Mediated Mineralization and Self-Similar Mesoscale-Organized Calcium Carbonate with Unusual Superstructures. *Adv. Mater.* **2008**, *20*, 1333–1338.

33. Kulak, A. N.; Iddon, P.; Li, Y. T.; Armes, S. P.; Cölfen, H.; Paris, O.; Wilson, R. M.; Meldrum, F. C. Continuous Structural Evolution of Calcium Carbonate Particles: A Unifying Model of Copolymer-Mediated Crystallization. *J. Am. Chem. Soc.* **2007**, *129*, 3729–3736.

34. Song, R. Q.; Xu, A. W.; Antonietti, M.; Cölfen, H. Calcite Crystals with Platonic Shapes and Minimal Surfaces. *Angew. Chem., Int. Ed.* **2009**, *48*, 395–399.

35. Mann, S.; Archibald, D. D.; Didymus, J. M.; Douglas, T.; Heywood, B. R.; Meldrum, F. C.; Reeves, N. J. Crystallization at Inorganic—Organic Interfaces—Biominerals and Biomimetic Synthesis. *Science* **1993**, *261*, 1286–1292.

36. Grassmann, O.; Lobmann, P. Morphogenetic Control of Calcite Crystal Growth in Sulfonic Acid Based Hydrogels. *Chem.—Eur. J.* **2003**, *9*, 1310–1316.

37. Andersen, F. A.; Brecevic, L. Infrared-Spectra of Amorphous and Crystalline Calcium Carbonate. *Acta Chem. Scand.* **1991**, *45*, 1018–1024.

38. Andersen, F. A.; Kralj, D. Determination of the Composition of Calcite—Vaterite Mixtures by Infrared Spectrophotometry. *Appl. Spectrosc.* **1991**, *45*, 1748–1751.

39. Albeck, S.; Aizenberg, J.; Addadi, L.; Weiner, S. Interactions of Various Skeletal Intracrystalline Components with Calcite Crystals. *J. Am. Chem. Soc.* **1993**, *115*, 11691–11697.

40. Davis, K. J.; Dove, P. M.; De Yoreo, J. J. The Role of Mg²⁺ as an Impurity in Calcite Growth. *Science* **2000**, *290*, 1134–1137.

41. Raz, S.; Weiner, S.; Addadi, L. Formation of High-Magnesian Calcites *via* an Amorphous Precursor Phase: Possible Biological Implications. *Adv. Mater.* **2000**, *12*, 38–42.

42. Braybrook, A. L.; Heywood, B. R.; Jackson, R. A.; Pitt, K. Parallel Computational and Experimental Studies of The Morphological Modification of Calcium Carbonate by Cobalt. *J. Cryst. Growth* **2002**, *243*, 336–344.

43. Mukkamala, S. B.; Anson, C. E.; Powell, A. K. Modelling Calcium Carbonate Biomineralisation Processes. *J. Inorg. Biochem.* **2006**, *100*, 1128–1138.

44. Orme, C. A.; Noy, A.; Wierzbicki, A.; McBride, M. T.; Grantham, M.; Teng, H. H.; Dove, P. M.; DeYoreo, J. J. Formation of Chiral Morphologies Through Selective Binding of Amino Acids to Calcite Surface Steps. *Nature* **2001**, *411*, 775–779.

45. DeOliveira, D. B.; Laursen, R. A. Control of Calcite Crystal Morphology by a Peptide Designed to Bind to a Specific Surface. *J. Am. Chem. Soc.* **1997**, *119*, 10627–10631.

46. Jimenez-Lopez, C.; Rodriguez-Navarro, A.; Dominguez-Vera, J. M.; Garcia-Ruiz, J. M. Influence of Lysozyme on the Precipitation of Calcium Carbonate: A Kinetic and Morphologic Study. *Geochim. Cosmochim. Acta* **2003**, *67*, 1667–1676.

47. Hernandez-Hernandez, A.; Rodriguez-Navarro, A. B.; Gomez-Morales, J.; Jimenez-Lopez, C.; Nys, Y.; Garcia-Ruiz, J. M. Influence of Model Globular Proteins with Different Isoelectric Points on the Precipitation of Calcium Carbonate. *Cryst. Growth Des.* **2008**, *8*, 1495–1502.

48. Fu, G.; Valiyaveettil, S.; Wopenka, B.; Morse, D. E. CaCO₃ Biomineralization: Acidic 8-kDa Proteins Isolated from Aragonitic Abalone Shell Nacre Can Specifically Modify Calcite Crystal Morphology. *Biomacromolecules* **2005**, *6*, 1289–1298.

49. Albeck, S.; Weiner, S.; Addadi, L. Polysaccharides of Intracrystalline Glycoproteins Modulate Calcite Crystal Growth *in Vitro*. *Chem.—Eur. J.* **1996**, *2*, 278–284.

50. MacKenzie, C. R.; Wilbanks, S. M.; McGrath, K. M. Superimposed Effect of Kinetics and Echinoderm Glycoproteins on Hierarchical Growth of Calcium Carbonate. *J. Mater. Chem.* **2004**, *14*, 1238–1244.

51. Mann, S. Molecular Tectonics in Biomineralization and Biomimetic Materials Chemistry. *Nature* **1993**, *365*, 499–505.

52. De Yoreo, J. J.; Dove, P. M. Shaping Crystals with Biomolecules. *Science* **2004**, *306*, 1301–1302.

53. Grassmann, O.; Muller, G.; Lobmann, P. Organic-Inorganic Hybrid Structure of Calcite Crystalline Assemblies Grown

in a Gelatin Hydrogel Matrix: Relevance to Biomineralization. *Chem. Mater.* **2002**, *14*, 4530–4535.

54. Yang, D.; Qi, L. M.; Ma, J. M. Well-Defined Star-Shaped Calcite Crystals Formed in Agarose Gels. *Chem. Commun.* **2003**, *10*, 1180–1181.

55. Zhan, J. H.; Lin, H. P.; Mou, C. Y. Biomimetic Formation of Porous Single-Crystalline CaCO₃ *via* Nanocrystal Aggregation. *Adv. Mater.* **2003**, *15*, 621–623.

56. Gebauer, D.; Volkel, A.; Cölfen, H. Stable Prenucleation Calcium Carbonate Clusters. *Science* **2008**, *322*, 1819–1822.

57. Morse, J. W.; Arvidson, R. S.; Luttge, A. Calcium Carbonate Formation and Dissolution. *Chem. Rev.* **2007**, *107*, 342–381.

58. Imai, H.; Terada, T.; Yamabi, S. Self-Organized Formation of a Hierarchical Self-Similar Structure with Calcium Carbonate. *Chem. Commun.* **2003**, *4*, 484–485.

59. Grassman, O.; Neder, R. B.; Putnis, A.; Lobmann, P. Biomimetic Control of Crystal Assembly by Growth in an Organic Hydrogel Network. *Am. Mineral.* **2003**, *88*, 647–652.

60. de Leeuw, N. H.; Parker, S. C. Surface Structure and Morphology of Calcium Carbonate Polymorphs Calcite, Aragonite, and Vaterite: An Atomistic Approach. *J. Phys. Chem. B* **1998**, *102*, 2914–2922.

61. R. Kniep, P. S. In *Biomineralization I: Crystallization and Self-Organization Process*; Springer-Verlag GmbH: Berlin, 2007; Vol. 270, p 73−125.

62. Addadi, L.; Raz, S.; Weiner, S. Taking Advantage of Disorder: Amorphous Calcium Carbonate and Its Roles in Biomineralization. *Adv. Mater.* **2003**, *15*, 959–970.

63. Politi, Y.; Arad, T.; Klein, E.; Weiner, S.; Addadi, L. Sea Urchin Spine Calcite Forms *via* a Transient Amorphous Calcium Carbonate Phase. *Science* **2004**, *306*, 1161–1164.

64. Xu, A. W.; Yu, Q.; Dong, W. F.; Antonietti, M.; Cölfen, H. Stable Amorphous CaCO₃ Microparticles with Hollow Spherical Superstructures Stabilized by Phytic Acid. *Adv. Mater.* **2005**, *17*, 2217–2221.

65. Gebauer, D.; Cölfen, H.; Verch, A.; Antonietti, M. The Multiple Roles of Additives in CaCO₃ Crystallization: A Quantitative Case Study. *Adv. Mater.* **2009**, *21*, 435–439.

66. Tjipto, E.; Quinn, J. F.; Caruso, F. Assembly of Multilayer Films from Polyelectrolytes Containing Weak and Strong Acid Moieties. *Langmuir* **2005**, *21*, 8785–8792.

67. Bergstrom, L. Hamaker Constants of Inorganic Materials. *Adv. Colloid Interface Sci.* **1997**, *70*, 125–169.

68. Cheng, X. G.; Gower, L. B. Molding Mineral within Microporous Hydrogels by a Polymer-Induced Liquid-Precursor (PILP) Process. *Biotechnol. Prog.* **2006**, *22*, 141–149.

69. Gower, L. B. Biomimetic Model Systems for Investigating the Amorphous Precursor Pathway and Its Role in Biomineralization. *Chem. Rev.* **2008**, *108*, 4551–4627.

70. Gower, L. B.; Odom, D. J. Deposition of Calcium Carbonate Films by a Polymer-Induced Liquid-Precursor (PILP) Process. *J. Cryst. Growth* **2000**, *210*, 719–734.

71. Hyde, S. T.; Andersson, S.; Larsson, K.; Blum, Z.; Landh, T.; Lidin, S.; Ninham, B. W. *The Language of Shape*; Elsevier: Amsterdam, 1997.

72. Manna, L.; Milliron, D. J.; Meisel, A.; Scher, E. C.; Alivisatos, A. P. Controlled Growth of Tetrapod-Branched Inorganic Nanocrystals. *Nat. Mater.* **2003**, *2*, 382–385.

73. Gehrke, N.; Cölfen, H.; Pinna, N.; Antonietti, M.; Nassif, N. Superstructures of Calcium Carbonate Crystals by Oriented Attachment. *Cryst. Growth Des.* **2005**, *5*, 1317–1319.

74. Wang, L. F.; Sondi, I.; Matijevic, E. Preparation of Uniform Needle-Like Aragonite Particles by Homogeneous Precipitation. *J. Colloid Interface Sci.* **1999**, *218*, 545–553.

75. Martyushev, L. M.; Kuznetsova, I. E.; Seleznev, V. D. Calculations of the Complete Morphological Phase Diagram for Nonequilibrium Growth of a Spherical Crystal under Arbitrary Surface Kinetics. *J. Exp. Theor. Phys.* **2002**, *94*, 307–314.

76. Huang, Y. X.; Buder, J.; Cardoso-Gil, R.; Prots, Y.; Carrillo-Cabrera, W.; Simon, P.; Kniep, R. Shape Development and Structure of A Complex (Otoconia-Like) Calcite−Gelatine Composite. *Angew. Chem., Int. Ed.* **2008**, *47*, 8280–8284.